Applied Thermal Engineering 199 (2021) 117604

Contents lists available at ScienceDirect

Applied Thermal Engineering

journal homepage: www.elsevier.com/locate/apthermeng

Machine learning and CFD for mapping and optimization of CO_2 ejectors

Knut Emil Ringstad [a,*], Krzysztof Banasiak [b], Åsmund Ervik [b], Armin Hafner [a]

[a] Norwegian University of Science and Technology, Kolbjørn Hejes vei 1B, 7491 Trondheim, Norway
[b] SINTEF Energy, Kolbjørn Hejes vei 1d, 7465 Trondheim, Norway

ARTICLE INFO

Keywords:
Computational fluid dynamics
Two-phase ejector
CO_2
Gaussian process regression
Optimization

ABSTRACT

In this study, a novel simulation-based algorithm for CO_2 ejector design and performance evaluation is presented. The algorithm is based on an automated Computational Fluid Dynamics (CFD) workflow that can account for different ejector geometries and operating conditions. The CFD data points are used to train a Gaussian Process Regression (GPR) machine learning model to predict the ejector performance indicators; efficiency, mass flow rates, outflow uniformity, and entropy generation. Three use cases are investigated using this methodology: 1) performance mapping for off-design operating conditions of a given ejector, 2) design mapping of ejector performance with 5 geometry variables investigated, and 3) flow structure prediction between different ejector mixing chamber geometries. The results show that this algorithm can be used to efficiently explore ejector designs with mean average errors between 0.07 and 0.1 [–] in entrainment ratio. Furthermore, the method can to look for optimized geometries using gradient descent methods, as well as produce ejector performance maps. Additionally, the method is able to predict local flow structures of velocity and pressure inside the ejector with varied ejector geometries. The databases and GPR method implementation from this work is made available open-source for further development and research.

1. Introduction

The urgent need to rapidly reduce greenhouse gas emissions calls for unprecedented action from individuals, industry, and governments. The Heating, Ventilation, Air-conditioning, and Refrigeration (HVAC & R) industry is accountable for a significant part of global greenhouse gas emissions. If not limited, large-scale adoption of high GWP synthetic working fluids like hydrofluorocarbons (HFCs) is expected to be a major contributor to global emissions within 2050 [1]. In response, international agreements to phase out high GWP working fluids have been ratified, such as the Kigali amendment to the Montreal Protocol and the EU F-gas regulation [2]. A promising alternative to the use of synthetic refrigerants is natural working fluids such as CO_2 (R744). R744 has a GWP of 1 and is a non-toxic, non-flammable, and natural refrigerant that can be efficiently implemented for many applications [3]. Furthermore, R744 has several favorable thermodynamic properties that allow for efficient and compact units. However, the high operating pressures common in R744 systems introduce large expansion losses, that can significantly reduce system COP. Therefore, expansion-loss recovery devices are often implemented to achieve higher system efficiency.

Ejectors are low-cost work-recovery devices with no moving parts that can use the lost expansion energy to pump a secondary flow to a higher pressure [4,5]. An ejector can improve system performance by as much as 10–30% [4] at design conditions. However, they are highly dependent on the correct design and minor changes in ejector geometry can dramatically reduce ejector efficiency [6–9]. Therefore, the development of efficient and accurate methods for ejector design has in recent years gained attention.

The flow within a two-phase ejector is challenging to model as it involves several interdependent and highly complex features such as compressible, super-sonic, and multiphase flow with phase change, and multiphase turbulence and flow jet atomization. Therefore, over the last decade, much research has been devoted to developing high-resolution CFD models to accurately predict ejector performance and improve their design. CFD models have seen extensive applications within R744 ejector design and performance prediction [10–16]. Today, the most commonly used model is the homogeneous equilibrium model (HEM). HEM models have been studied extensively [17,18,12,13,10,19,11,16,5,14] and can reasonably predict motive mass flow rates (MFR) for supercritical motive conditions [5]. For better prediction of the motive mass flow rate at lower motive inlet pressure conditions Palacz et al. [12] concluded that non-equilibrium effects should be considered. In general, CFD models are able to accurately

* Corresponding author.
E-mail address: knut.e.ringstad@ntnu.no (K.E. Ringstad).

https://doi.org/10.1016/j.applthermaleng.2021.117604
Received 31 May 2021; Received in revised form 30 July 2021; Accepted 16 September 2021
Available online 27 September 2021

Nomenclature

Abbreviations

ANN	Artificial Neural Network
CFD	Computational fluid dynamics
EoS	Equation of state
GP	Gaussian Process
GPR	Gaussian process regression
GWP	Global warming potential
HEM	homogeneous equilibrium model
HFC	Hydrofluorocarbon
HRM	Homogeneous relaxation model
HVAC	Heating, ventilation, air-conditioning, and refrigeration
KPI	Key performance indicator
LHC	Latin hyper cube
MFR	Mass flow rate
MSE	Mean squared error
ROM	Reduced Order Model
UDF	User defined function

Symbols

α_d	Diffuser angle
$\overline{E}$	Expectation value
χ	Scaled sampling variable
$\dot{S}_{h1,2,3}$	Enthalpy source term
ϵ	Turbulent kinetic energy dissipation
η	Efficiency
Γ	Diffusion coefficient
λ	Thermal conductivity
μ	viscosity
ϕ	vapour volume fraction
ψ	Generic field variable
ρ_m	Density
σ	Data variance
τ	Stress tensor
θ	Hyperparameter
$\overline{u}$	Velocity vector
c_p	heat capacity
D_{diff}	Diffuser outlet diameter
$D_{\text{m-out}}$	Motive outlet diameter
D_{mix}	Mixing chamber diameter
L_{mix}	Mixing chamber length
T	Temperature
a	Sampling range
E	Total Energy
f	Underlying unobservable function
G	Learning rate
h	Enthalpy
K	Covariance function - kernel
k	Turbulent kinetic energy
l	Characteristic length scale
M	Data mean
n	Noise
P	Pressure
Pr	Prandtl number
q	Heat flux
s	Entropy
W	Work
x	Direction vector
X,y	Data in dataset

Subscripts

eff	Effective
i,j	Notation indices
m	Motive
m	Pseudo-fluid mixture property
o	Outlet
s	Suction
t	Turbulent

predict motive MFR typically within 10%. However, the suction MFR is less accurately predicted, with errors ranging up to 20–100%. For a detailed review on ejector modeling, its applications, and available experimental data, the reader is referred to Ringstad et al. [5].

While the high sensitivity of ejector performance to their design has been noted in several studies[6,7,14], major knowledge gaps remain in the field of high-performance ejector design. Nakagawa et al. [6] investigated the effect of different mixing chamber geometries experimentally, noting the significant impact of the mixing chamber length on ejector performance. This was followed up in the work by Banasiak et al. [7] and Banasiak et al. [15] where the mixing chamber and diffuser geometries were investigated experimentally and numerically. They concluded that these geometry parameters were important for achieving high ejector efficiency and that the most important parameters for ejector performance were the mixing chamber diameter, both with a significant impact on entropy production. Furthermore, they concluded that the different parameters must be optimized simultaneously and not in isolation. Entropy production in R744 ejectors was further investigated by He et al. [14] using CFD. The results showed that the motive outlet diameter plays a critical role in ejector performance and that the nozzle exit position plays a key role in momentum exchange and exergy destruction.

In this work, a method for producing a machine learning-based surrogate model from numerical results is presented. Using this surrogate model, it is possible to replace several different calculation tools with a single one. Here, three distinct cases are presented (1) performance mapping for different operating conditions given a specific ejector geometry, (2) design mapping and optimization of ejector performance with different geometric parameters, (3) flow structure mapping for different ejector geometries.

Performance mapping of off-design performance has been investigated using CFD in previous works by Haida et al. [20,11]. CFD data was used to generate a Reduced Order Model (ROM) to quickly predict ejector performance at any operating condition. Such ROM models has great applicability for dynamic simulations [11] or Digital Twins.

CFD based shape optimization for R744 ejectors has been previously carried out by Palacz et al. [12,13], resulting in the EjectorPL system for automated CFD model generation. The study compared two evolutionary optimization approaches for ejector design. The results showed that up to 6% improvement in ejector efficiency is possible from an existing design based on 1D model calculations. Barta et al. [21] recently presented a design optimization methodology for R744 ejectors based on 0D sub-component polynomial modeling. The methodology can accurately predict ejector performance and offers insights into design trade-offs in ejector design.

Alternatively, optimization may be performed on performance maps using optimization methods such as gradient descent. This, however, depends on quick evaluation of results and their gradient at any given point in the design space. For complex flow devices, such as ejectors, evaluating the flow at a single design point with CFD tools requires significant computational effort (from hours to days). Therefore, it is better to perform the optimization on a surrogate meta-model such that performance can be quickly evaluated.

In this work, the Gaussian Process Regression (GPR) machine

learning approach is used to generate such a surrogate model from a large set of CFD data. The CFD database is built using an automated workflow for different shape designs, model parameters, and operating conditions. Using CFD results to generate a large database has several advantages. Firstly, it enables one to investigate local flow structures in detail. Secondly, CFD models implicitly take into account 2D or even 3D geometric effects which are impossible to account for using simpler zero or one-dimensional approaches.

The datasets are used for the training of a Gaussian Process Regression model to predict different ejector performance indicators and flow structures inside the ejector. GPR has been extensively used for a wide range of model problems [22]. Alternative machine learning methods, such as artificial neural networks (ANN), have previously been used in ejector design [23] and performance analysis [24,25]. Still, GPR models have advantages over ANN methods, such as more efficient use of data, lower risk of overfitting, ease of use, and explainability [26].

Using this GPR surrogate modeling approach, both performance- and shape mapping are handled with one tool. This simplification also allows for combined studies of shape and operating conditions in a novel way. In addition, the mapping can be used for the optimization of both operating conditions and geometry. This approach has several advantages over other methods:

1. It can give a full mapping of performance at any combination of parameters, allowing for a full investigation of possible designs and what-if scenarios.
2. The method can take advantage of experimental and numerical results from previous works to improve model accuracy.
3. The GPR method provides estimated prediction uncertainty at any point. This information can be used to improve modeling tools or refine database coverage.
4. The method can produce maps of local flow structures with varied geometries and operating conditions.

2. Ejector CFD model

2.1. Multiphase model

In this work, the multiphase flow within a two-phase R744 ejector is modeled using a homogeneous equilibrium model (HEM) based on the formulation of Smolka et al. [17]. The HEM is based on the assumption of strongly coupled phases at mechanical, thermal, and thermodynamic equilibrium, i.e. both phases can be described with a single velocity-($\vec{u}$), temperature- (T), and pressure-field (P). By these assumptions, a single set of partial differential equations for the mixture of liquid and gas needs to be solved. Essentially, the two phases are then treated as a single pseudo-fluid with transport properties derived according to an averaging procedure. This pseudo-fluid will be governed by the equations of fluid motion and energy:

$$\frac{\partial \rho_m}{\partial t} + \frac{\partial}{\partial x_j}\left[\rho_m u_{mj}\right] = 0, \tag{1}$$

$$\frac{\partial}{\partial t}\left(\rho_m u_{mi}\right) + \frac{\partial}{\partial x_j}\left[\rho_m u_{mi} u_{mj} + P\delta_{ij} - \tau_{ij\_\mathrm{eff}}\right] = 0, \tag{2}$$

$$\frac{\partial}{\partial t}\left(\rho_m E_m\right) + \frac{\partial}{\partial x_j}\left[\rho_m u_{mj} h_m - q_{j,\mathrm{eff}} - u_{mi}\tau_{ij,\mathrm{eff}}\right] = 0, \tag{3}$$

Here the Einstein notation is used with subscript-indexes i and j, and the subscript m indicates the pseudo-fluid mixture properties. Here, ρ_m, u_m, P, E, h_m, q refer to the density, velocity, pressure, total energy, mixture enthalpy and heat flux, respectively. The effective stress tensor $\tau_{ij,\mathrm{eff}}$ is the laminar (Newtonian) and turbulent stress tensors combined:

$$\tau_{ij,\mathrm{eff}} = \tau_{ij} + \tau_{ij,\mathrm{t}}. \tag{4}$$

To obtain the total mixture enthalpy, an alternative formulation of the energy equation, Eq. (5), was implemented using user-defined functions (UDF) in the ANSYS Fluent software [27], replacing Eq. 3.

$$\frac{\partial}{\partial t}\rho h + \nabla\cdot\left(\rho\vec{u}h\right) = \nabla\cdot\left(\Gamma_{\mathrm{eff}}\nabla h\right) + \dot{S}_{h1} + \dot{S}_{h2} + \dot{S}_{h3} \tag{5}$$

In this equation, h is the specific enthalpy, $\vec{u}$ is the velocity vector, Γ_{eff} the effective diffusion coefficient. The source terms $\dot{S}_{h1,2,3}$ describe the mechanical energy, the irreversible dissipation of the kinetic energy variations, and the dissipation of the turbulent kinetic energy, respectively [17].

Γ_{eff} is defined as:

$$\Gamma_{\mathrm{eff}} = \frac{\mu_t}{Pr} + \frac{\lambda}{c_p}, \tag{6}$$

where μ_t is the turbulent viscosity, Pr is the Prandtl number, c_p is the mixture specific heat capacity, and λ is the thermal conductivity.

2.2. Equation of state

One preferable property of the equilibrium assumption is that the pressure and enthalpy uniquely define the thermodynamic state, and thus the properties in the two-phase dome. Properties are typically divided into thermophysical (Eq. 7) and transport (Eq. 8) properties.

$$\begin{bmatrix}\rho\\ c_p\\ \phi\\ T\\ s\end{bmatrix} = f\begin{pmatrix}P, h\end{pmatrix}, \tag{7}$$

$$\begin{bmatrix}\mu\\ \lambda\end{bmatrix} = g\left(P, h\right), \tag{8}$$

where $\rho, \phi, \mu, \lambda, c_p, s$ are the pseudo-fluid density, vapour volume fraction, kinematic viscosity, thermal conductivity, specific heat capacity, and specific entropy, respectively.

The properties of liquid and gas are evaluated by the pressure and enthalpy, interpolated from a look-up table. The CoolProp library [28] for R744 is based on the Span-Wagner equation of state, which is considered the most accurate equation of state (EoS) for CO_2 and is widely used for R744 ejector simulations [5]. Here, CoolProp is used to generate the look-up tables that are imported in Fluent using UDFs. This study is limited to the operating range suited for the HEM model, however, the methods presented here are easily extended to cover non-equilibrium conditions.

2.3. Turbulence model

Accurately describing the mixing process inside two-phase ejectors is largely dependent on modelling the two-phase turbulent flow inside the mixing chamber. The turbulent viscosity, μ_t, is then sub-modeled by the $k-\epsilon$ realizable turbulence model. This model involves solving the set of transport equations for the turbulent properties, Eqs. (9) and (10):

$$\frac{\partial}{\partial t}\left(\rho_m k\right) + \frac{\partial}{\partial x_j}\left(\rho_m k u_{mj}\right) = \frac{\partial}{\partial x_j}\left[\left(\mu + \frac{\mu_t}{\sigma_k}\right)\frac{\partial k}{\partial x_j}\right] + p_k + p_b - \rho\epsilon - \mathrm{Y_M} + \mathrm{S_k}, \tag{9}$$

$$\frac{\partial}{\partial t}\left(\rho_m \epsilon\right) + \frac{\partial}{\partial x_j}\left(\rho_m \epsilon u_{mj}\right) = \frac{\partial}{\partial x_j}\left[\left(\mu + \frac{\mu_t}{\sigma_\epsilon}\right)\frac{\partial \epsilon}{\partial x_j}\right] + \rho C_1 S\epsilon - \rho_{\mathrm{m}} C_2 \frac{\epsilon^2}{\mathrm{k} + \sqrt{\mu\epsilon}/\rho_{\mathrm{m}}} + C_{1\epsilon}\frac{\epsilon}{\mathrm{k}} C_{3\epsilon} \mathrm{p_b} + \mathrm{S}_\epsilon, \tag{10}$$

$$\mu_t = \rho_m \frac{k^2}{\epsilon}, \tag{11}$$

where the subscript, m, indicates mixture properties based on mass or volume weighted averaging, C is a model specific constant, S and Y are model specific source terms, p is the strain rate production of k; $p = \mu_t E_{ij} E_{ij}$. This model has favourable stability properties in comparison to k-ω based models and scalable wall functions simplifies the automated meshing algorithm [5].

3. Machine learning approach

3.1. Gaussian process regression

Gaussian Process Regression (GPR) is a supervised machine learning tool based on Bayesian regression to generate surrogate models. The model is trained using a labeled data set $(y_i, \mathbf{X}_i)$, where y is the observations, and X is the input for datapoint i. The data used in the machine learning model are referred to as features. The feature data is rescaled to be zero mean with unit variance, according to Eq. (12), using the Sklearn toolset StandardScaling [29]:

$$z = \frac{X - M}{\sigma} \tag{12}$$

Here, X and z are the unscaled and scaled feature data, respectively, μ is the feature data mean, and σ is the feature data standard deviation.

Assuming that the observations are obtained from an unobservable underlying function f with zero mean Gaussian noise, $n_i = \mathcal{N}(0, \sigma)$, the input-output relationship can be written as (Eq. 13):

$$\mathbf{y} = f(\mathbf{X}) + n_i \tag{13}$$

The Gaussian Process (GP) can then be written as (Eq. 14):

$$\mathbf{y} = \mathcal{GP}(M(X), K(X, X'; \theta)) \tag{14}$$

The GP has a mean function, $M = \overline{E}[f(X)]$, where $\overline{E}$ is the expectation value, a covariance function $K(X, X') = \overline{E}[f(X)f(X')]$, and a set of model hyperparameters θ. The co-variance function is also referred to as the kernel, which measures the correlation between the outputs variable at two points X_i, X_j, and is specified as a prior.

In this paper, the Squared Exponential kernel is used as a covariance function and a white noise kernel is added to account for numerical errors. The combined kernel function is then defined as (Eq. 15):

$$K\left(X, X'; \theta, \sigma\right) = \sigma_f^2 \exp\left(-\frac{1}{2l^2}(X - X')^2\right) + \sigma_n^2 \mathbb{I} \tag{15}$$

where, $\mathbb{I}$ is the identity matrix. The kernel has three hyper parameters; σ_f, l, and σ_n, which are the signal standard deviation, the characteristic length-scale, and the noise level (variance) respectively. The parameter σ_f is a scaling parameter and the length-scale l governs the length over which two points X and X' are correlated. Larger values of l enforces that f varies more smoothly. The characteristic length scale is dimensional and can vary between features.

Hyperparameters (l, σ_n, σ_f) are optimized during the fitting of the data using a gradient descent optimizer on the log-marginal-likelihood of the hyper-parameters. The optimizer is a quasi-Newton L-BFGS optimizer [30,29,31] with $n = 10$ optimizer restarts, commonly used in the literature [32]. Characteristic length scales are bounded to upper and lower limits of 1.0×10^{-3} and 3.0×10^{1}, respectively, for all dimensionless features. The kernel optimizer is initialized with $\sigma_{f,0} = 0.2, l_0 = 0.5$, $\sigma_{n,0} = 0.02$. Using the training data with dimensions A × (B_{total} - $B_{training}$), where A is the number of features and B the number of data points, a posterior distribution can be found by drawing from a joint distribution of the training data y and test data $y*$.

$$\begin{bmatrix} y \\ y* \end{bmatrix} = \mathcal{N}\left(\begin{bmatrix} M \\ M* \end{bmatrix}, \begin{bmatrix} K & K^* \\ K^* & K^{**} \end{bmatrix}\right) \tag{16}$$

This GPR algorithm was implemented using the Scikit-learn Python package [29].

3.2. Gradient descent based optimization

The GPR model predicts the ejector operation at any point in the defined feature domain. By using a gradient-based optimization algorithm on the function it is possible to optimize the ejector parameters for a given output. Here, a gradient descent optimization algorithm was implemented according to, Eq. (17):

$$\mathbf{X}_{i+1} = \mathbf{X}_i + G\nabla f(\mathbf{X}_i) \tag{17}$$

Here, G is a specified learning rate and f is the chosen function to optimize. A first-order finite difference method for evaluating the gradient. The initial points were chosen randomly from a uniform distribution of the feature space.

4. CFD automation algorithm

To generate the data sets needed to train the GPR model, an algorithm was developed in the Python 3.9 programming language [33] for automatically generating CFD data. This algorithm incorporates automatic meshing, automatic generation of Fluent journal files, and post-processing the results. An illustration of the system layout is presented in Fig. 1. The program takes in data points from the boundary condition - geometry design space and automatically simulates the flow case.

Initially, the automated algorithm settings need to be defined. This involves choosing the features to be explored and choosing the remaining constant parameters. In this step, different sampling algorithms, meshing strategies, and post-processing settings are available. Based on the chosen features and sampling algorithms, a user-specified number of data points are sampled from the design space. The sampling algorithm used is further discussed in Section 4.1. The algorithm then iteratively simulates each flow case in three steps.

The first step is to generate the specified 2D structured mesh using an in-house automated meshing script for the ICEM meshing program according to the specified geometry parameters. The script generates high-quality meshes with average orthogonal quality of 99.9% for a 10k cell mesh. The mesh parameters included are the baseline cell size, refinement ratio, and aspect ratio of the mixing section cells. A mesh sensitivity study is conducted and discussed in Section 4.3.1. Acceptable results were obtained using meshes around 8k cells. To limit computational cost while keeping the high accuracy a mesh of 24k cells was chosen as the average design case.

The second step is to generate an ANSYS Fluent journal file to automatically run the flow case with the prescribed boundary conditions from the algorithm for pressure and enthalpy. The inlets and outlets were prescribed with the ANSYS pressure-inlet and pressure-outlet boundary conditions, respectively. The boundary conditions for the specific enthalpy defined for the HEM model were zero gradient enthalpy at the outlet and constant inlet enthalpy. The wall conditions were defined as adiabatic with a wall roughness of $H_{rough} = 2[\mu m]$, commonly used in CFD literature for R744 ejectors [13,34]. All calculations were done using a steady solver. The discretization schemes used are described in Table 1.

Each case is simulated in ANSYS Fluent 2019R3 with the standard initialization procedure, starting the simulations with first-order schemes for the first 20k iterations, before changing to second-order schemes. Convergence was judged based on low mass flow rate imbalance below 1.0×10^{-5} [kg/s] and residuals below 1.0×10^{-5}. The majority of the simulations would converge within 40–50k iterations. Simulations that did not converge were continued until either conver-

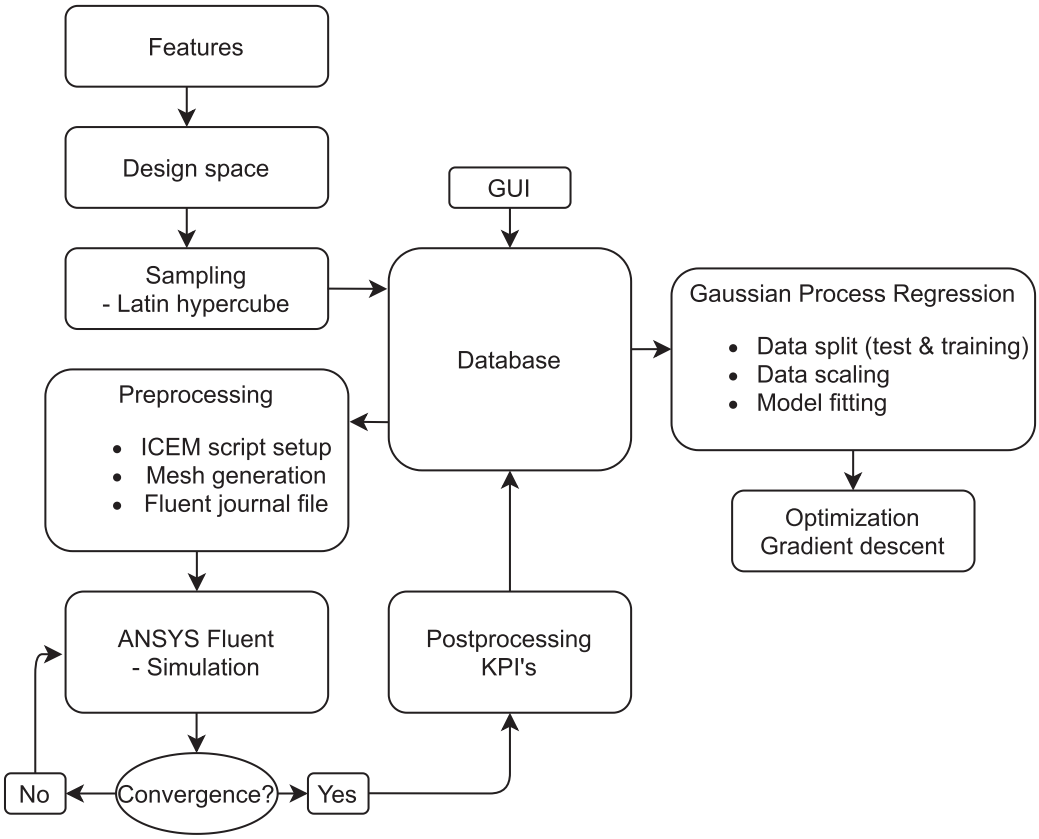

Fig. 1. Illustration of the algorithm layout.

Table 1
Discretization schemes used in the CFD models.

Discretization	Scheme
Pressure	PRESTO!
Pressure-velocity coupling	Coupled
Gradient	Green Gauss cell-based
Momentum	Second order upwind
Density	–"–
Enthalpy	–"–
Turbulent kinetic energy	–"–
Turbulent energy dissipation	–"–

gence or reaching 80k iterations. Simulations that were oscillating after 80k iterations were removed from the results. These oscillations typically occurred at low motive inlet specific enthalpy (below 270 [kJ/kg]) and high motive pressures (above 110 [bar]), which is close to the limit of the HEM range of validity.

The third step is to post-process the CFD results, collecting the different output KPI parameters and storing these in a database. The different output parameters and their calculation are discussed in Section 4.2. After all the steps are completed the database is stored and duplicated. After which the data can be analyzed by the machine learning model.

4.1. Sampling

The design space is initially sampled using a Latin HyperCube (LHC) approach [35] with the Python package LHC-Python. Latin hypercube sampling is a statistical sampling approach that samples N points from a statistical distribution in equiprobable zones. This approach ensures good sampling of a higher dimensional subspace with fewer data points than random or equidistant sampling. The LHC design gives an N-dimensional mapping to fill a space with low overlap. The design points χ_i are chosen from the range (0,1) and is transformed to a chosen subspace for each feature, x_i. All variables are sampled evenly according to Eq. (18),

$$X_i = \chi_i * (a_{\max} - a_{\min}), \tag{18}$$

using the maximum and minimum values, $a_{\min/\max}$, presented in Table 2. This is to get a well-represented operational mapping for different given ejectors.

To avoid sampling unphysical ejector geometry combinations a sampling constraint had to be added. The motive outlet diameter was constrained such that the motive nozzle is smaller than the suction chamber at the nozzle exit position according to:

$$D_{\mathrm{m-out}} < 2(tan(\alpha_s/2)L_{\mathrm{mch}} + D_{\mathrm{mix}}/2 - t) \tag{19}$$

Table 2
Available features and their parameter sampling range for LHC-sampling algorithm.

Parameter	$a_{\min}$	$a_{\max}$
$D_{\mathrm{m-out}}$, [mm]	D_{throat}	1.5 D_{throat}, Eq. (19)
L_{mix}, [mm]	0	50 D_{mix}
D_{mix}, [mm]	D_{throat}	10 D_{throat}
D_{diff}, [mm]	D_{mix}	10 D_{mix}
α_{d}, [°]	1	90
P_m, [bar]	75	140
P_s, [bar]	28	55
P_o, [bar]	P_s	P_s+15
h_m, [kJ/kg]	250	340
h_s, [kJ/kg]	380	460

4.2. Key performance indicators

In this study, four Key Performance Indicators (KPIs) were considered to evaluate ejector performance for different ejector designs. These are motive and suction mass flow rates (entrainment ratio), ejector efficiency, mixture entropy generation rate, and ejector outlet flow uniformity for velocity and vapor fraction.

Mass flow rates are calculated by Fluent at the inlets and outlets of the ejector. These are reported and post-processed by the algorithm. Using the mass flow rates and boundary conditions, the ejector efficiency is calculated from the Elbel efficiency, Eq. (20) [36] using calls to the CoolProp software [28].

$$\eta_{\text{ejector}} = \frac{\dot{W}_{\text{r}}}{\dot{W}_{\text{r,max}}} = \omega \cdot \frac{h(P_{\text{out}}, s_{\text{s}}) - h_s}{h_m - h(P_{\text{out}}, s_m)} \tag{20}$$

Entropy production is found by calculating the mass-weighted average of the incoming and outgoing entropy in each section. This is done using surface definitions and an entropy look-up table implemented in ANSYS Fluent using user-defined functions. The ejector outlet flow uniformity is calculated using the Uniformity Index defined in ANSYS Fluent:

$$\gamma_a = 1 - \frac{\sum_{i=1}^{n} \left(\left| \psi_i - \overline{\psi}_a \right| \right) A_i}{2 \left| \overline{\psi}_a \right| \sum_{i=1}^{n} A_i} \tag{21}$$

where $\overline{\psi}_a$ is the averaged value of the field variable ψ over the n cells on the outlet surface, and A_i is the surface area for cell i. Here, the unformity index is calculated for the vapour fraction ϕ and the axial velocity u. These two KPIs indicate how well mixed the flows are at the outlet of the ejector.

4.3. CFD model validation

The HEM as implemented in this work has been extensively validated in previous works [17,37,38]. As previously mentioned, the prediction error of the presented model is typically considered to be within 10% for motive mass flow rate. Suction mass flow rate is less accurately predicted, and can in cases significantly deviate from experimental results. Therefore, simulation results and any optimized design should be carefully inspected and scrutinized. This also motivates further research into the modeling of R744 two-phase ejectors. The presented methodology is modular, and switching the underlying CFD model can be done with only minor modifications.

4.3.1. Mesh sensitivity study

To ensure that the mesh is sufficiently refined to describe the ejector flow and mesh independent results are achieved a mesh study was conducted. The main ejector geometry parameters are presented in Table 3. This ejector geometry is intended as an open-access geometry for simulations as sharing of this geometry is not limited by proprietary restrictions. The different ejector dimensions are illustrated in Fig. 2.

Table 3
All main ejector dimensions of the new proposed open design.

Parameter	Value
Motive Inlet diameter ($D_{\text{m-in}}$)	10.0 [mm]
Motive Throat diameter (D_{throat})	1.41 [mm]
Motive Outlet diameter ($D_{\text{m-out}}$)	1.52 [mm]
Nozzle tip thickness (t)	1.2 [mm]
Pre-mixer length (L_{mch})	4.2 [mm]
Mixer length (L_{mix})	26.0 [mm]
Mixer diameter (D_{mix})	4.0 [mm]
Diffuser diameter (D_{diff})	12.0 [mm]
Diffuser angle (α_{d})	6[°]
Motive converging angle ($\alpha_{\text{m-c}}$)	35[°]
Motive diverging angle ($\alpha_{\text{m-d}}$)	3[°]
Suction angle (α_{s})	42[°]

Previous studies with the HEM have investigated mesh independence and shown that mesh independent results can be achieved with only 9k cells for optimization studies [13]. The ejector simulations were performed with five different meshes, A, B, C, D, E that were composed of 2.2k, 8k, 26k, 60k, and 100k cells, respectively. Meshes A, B, and E were generated using an ICEM mesh refinement algorithm for coarsening and refinement of mesh C. The refinement is applied uniformly for all cells, halving/doubling the mesh size in each dimension. Mesh D was based on a smaller baseline cell size in the meshing script with a similar refinement to mesh C. These simulations were run with boundary conditions named OP1[1] close to the design point, see the footnote. The calculated mass flow rates are presented in Table 4. The motive mass flow rate tends to reduce with the mesh refinement. However, the difference between these flow rates was less than 5% for all mesh densities. The suction mass flow rate varied more than the motive MFR, and has, in general, a decreasing trend as the mesh is refined. The suction mass flow rate is less accurately predicted with mesh A, 11% difference to mesh E, while for mesh B and C the difference is less than 1%. Interestingly, mesh D produced higher suction MFR than the other meshes. This could be due to that mesh D is based on a different baseline cell size.

Based on these mesh refinement indicators mesh C was chosen for further study, as it gave reasonable accuracy, within 1% of the most refined mesh, with a low computational cost. The study shows that R744 ejector flow using the HEM can be reproduced with a coarse mesh, which agrees with previous findings by Palacz et al. [13]. Such a mesh is ideal for use in optimization algorithms where computational speed is essential.

5. Results and discussion

The presented method is flexible and can look at various combinations of features. Any computable and physical combination of geometry variables, operating condition parameters, or CFD model parameters can be used for the mapping. In addition the GPR model can be applied for the prediction of flow structures such as pressure and velocity distributions, entropy production, and flow separation. Here, the results of the methodology are presented for three use cases. Case 1; generate an operation map for off- and on-design conditions using a given ejector geometry. Case 2; design space mapping and optimization at a given operating condition. Case 3; prediction of flow structures in the ejector from CFD data. Other use cases with alternative features are presented and discussed in Section 6.

5.1. Case 1: Off-design operation mapping

Case 1 presents a method of performance mapping of a given design at various operating conditions. Only the thermodynamic features (P_m, P_s, P_o, h_m, h_s, see Table 2) are included in this part of the investigation. These features are allowed to vary as specified in Table 2. The ejector geometry used is the new ejector geometry presented in Table 3.

5.1.1. Database sampling

Model accuracy is dependent on the number of data points. To verify how accuracy is affected by the number of data points, a model convergence study is done. One can test the sensitivity to the number of data points by either removing points from the training set or by generating additional data with more points. As each database is generated with an LHC sampling method, a fair comparison cannot be

[1] OP1: P_m = 85 [bar], P_s = 33 [bar], P_o = 38 [bar], h_m = 290 [kj/kg], h_s = 432 [kj/kg]

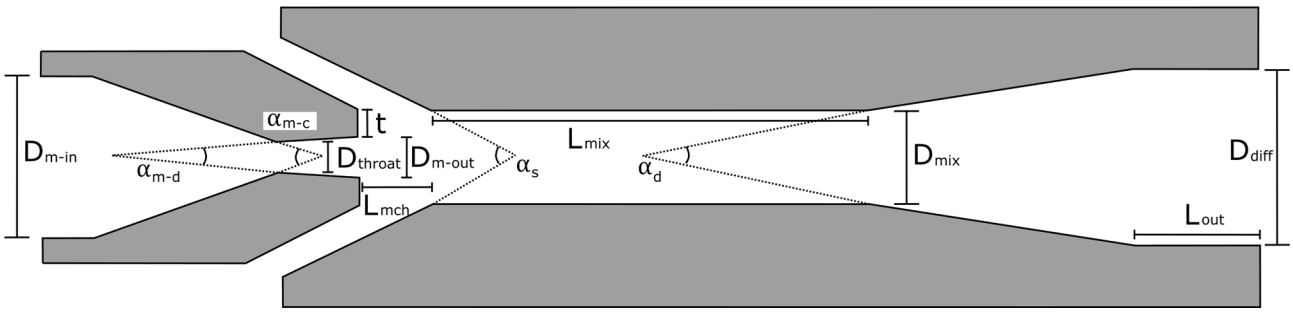

Fig. 2. Generic ejector geometry with geometry parameters. Gray color signifies solid parts.

Table 4
Mesh convergence study with different mesh sizes.

Mesh	Cells	OP1 [kg/s]	
		MFR_m	MFR_s
A	2.2k	0.0824	0.0538
B	8.0k	0.0812	0.0615
C	26k	0.0799	0.0613
D	62k	0.0795	0.0662
E	100k	0.0791	0.0609

made by simply removing data points. Therefore, three separate databases of 100, 300, 600 data points were sampled and simulated. The GPR model was trained using these three databases and the average GPR model accuracy was evaluated with different test and training sampling sizes. The mean squared error (MSE) between the GPR model prediction and the CFD data points in the test data was calculated for the different KPIs. The errors are estimated using 15% of the data as hidden test data that is left out of the model training and 85% as training data. The calculated mean square error results are shown in Fig. 3, normalized by the error with the smallest dataset.

From Fig. 3 it is found that, except for entropy, all KPIs are better predicted by increasing the database resolution. Refining the database to 600 datapoints reduced the MSE by 50–90% for the different KPIs. Interestingly, entropy production in the mixing chamber is worse resolved as the number of points is increased. This is believed to be caused by small length scales associated with the entropy production that are not resolved by the smaller data sets. Improved entropy post-processing models for entropy [39] should be implemented in further work to gain better data and insights into entropy production mechanisms in the flow.

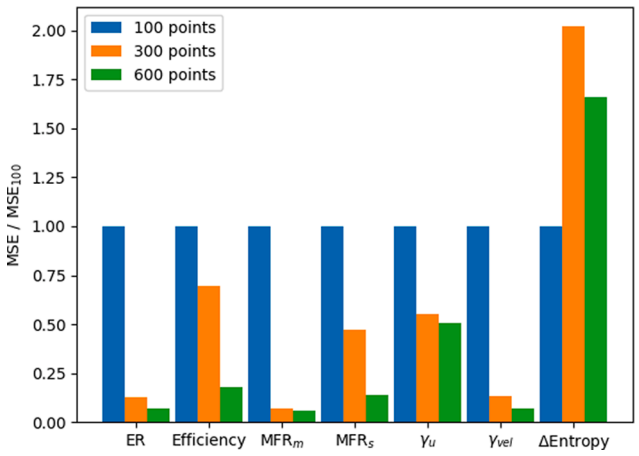

Fig. 3. Comparison of database sizes and the GPR prediction mean-square error for each KPI. The data has been non-dimensionalized by the mean square error for the 100 data point set.

Still, with only 100 data points, the algorithm can accurately calculate a performance map. The average absolute error for entrainment ratio was found to vary between 0.25 and 0.35 [–] with 100 data points, and vary between 0.06 and 0.1 [–] with 600 data points. Using a larger database could ensure even better accuracy of the GPR model, however, due to computational limitations, the study is limited to a 600 point database. The 600 data point set will be analyzed in the following sections as it gave the highest accuracy.

5.1.2. Model prediction

The GPR model can predict the ejector performance at any combination of features, however, its accuracy depends on the proximity to a nearby data point. The predictions can be used to generate a heat-map of ejector performance by varying two features and keeping the remaining constant. Such a performance mapping is presented in Fig. 4a–c in a motive condition P-h diagram using one realization of the GPR model. Here, the features for motive pressure and motive enthalpy are investigated, keeping the remaining features at constant conditions, specified in each figure caption. As shown in Fig. 4a, the model identifies a high-efficiency region near 120–140 [bar] at an enthalpy between 270 and 320 [kJ/kg] for high-pressure lifts (10 [bar]). Here, ejector break-down (no suction flow) occurs for lower motive pressure than 90 [bar]. As the pressure lift is reduced to 7 [bar], Fig. 4b, the high-efficiency region is extended to pressures between 100 and 130 [bar]. Below 100 [bar] the ejector performance quickly drops off and ejector break down occurs for pressures lower than 80 [bar]. As the pressure lift is reduced to 3 [bar], Fig. 4b, the optimum operating point moves to a smaller region closer to 90 [bar]. At low-pressure lifts, using higher pressures than 90 [bar] is not valuable in terms of ejector efficiency. The presented mapping can indicate zones that are optimal operation points for the presented ejector. Furthermore, these performance maps can be easily implemented into dynamic system simulations as a performance evaluation can be calculated within milliseconds.

5.1.3. Performance mapping - characteristic length scales

The GPR model optimizes the characteristic length scales (l in Eq. 15) for each parameter. If a feature is associated with a short characteristic length scale, the data contains more variation in that parameter. When a feature is associated with a characteristic length scale that is large compared to the feature space, then this feature is redundant to predict an output. Table 5 shows the different obtained characteristic length scales for one run of the GPR model. Characteristic length scales were limited to an upper limit of 30 standard deviations in scaled form. Based on these results, some relationships are suggested. First, the motive mass flow rate is primarily governed by the motive enthalpy (temperature) and pressure. This is reasonable as, for a chocked super-sonic flow, the upstream temperature and the upstream and downstream pressure are the primary parameters for the mass flow rate. It was expected that the outlet pressure would have a more significant impact on results, however, these results might indicate that the sampling range for outlet pressure was too small for this effect to be dominant. Second, void fraction uniformity is independent of the performance of the ejector,

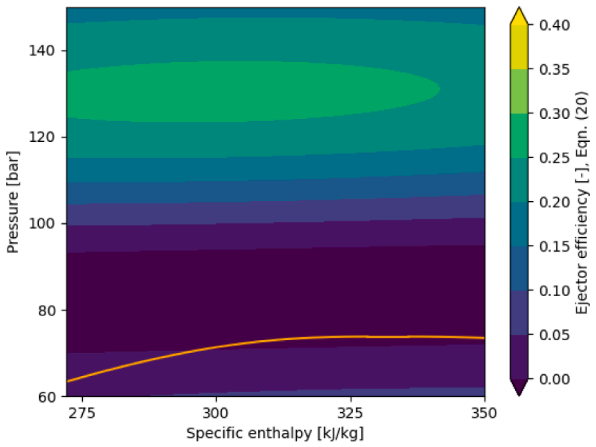

(a) Efficiency contour plot at conditions: $P_s = 35$ [bar], $P_{lift} = 10$ [bar].

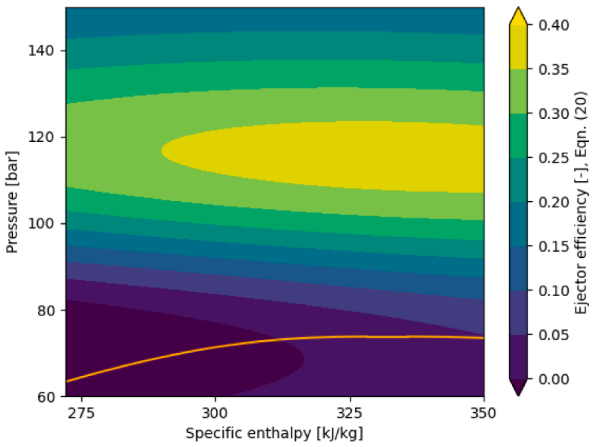

(b) Efficiency contour plot at conditions: $P_s = 38$ [bar], $P_{lift} = 7$ [bar].

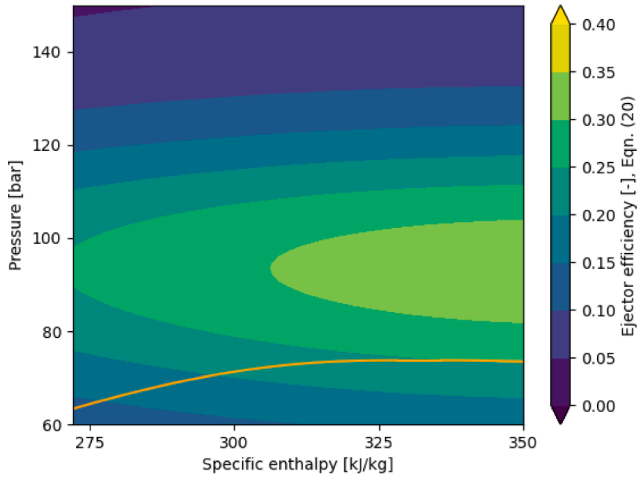

(c) Efficiency contour plot at conditions: $P_s = 42$ [bar], $P_{lift} = 3$ [bar].

Fig. 4. Efficiency (Eq. 20) map in a P-h diagram for motive conditions at different pressure lifts. Saturation line for CO_2 plotted in orange in each subfigure. Suction inlet specific enthalpy is kept constant at 430 [kJ/kg].

Table 5
Optimized characteristic length scales for different outputs. Kernel seed = 40

	Optimized characteristic length scale for feature				
Output parameter	P_m	P_o	P_s	h_m	h_s
Entrainment ratio [–]	2.17	1.65	2.05	2.71	30
Efficiency [–]	1.21	0.342	0.316	3.07	30
MFR_m [kg/s]	5.01	30	30	4.42	30
MFR_s [kg/s]	4.04	2.6	3.88	2.2	30
Velocity uni., [–]γ_u	4.21	3.31	4.28	30	30
Void frac. uni., γ_ϕ [–]	30	30	30	30	30
Entropy prod., ds_{m-d} [–]	1.65	3.17	4.35	12.8	7.63

however, this is found to be caused by the void fraction always being highly uniform at diffuser exit. Third, velocity uniformity is governed primarily by the pressures at the ejector ports and is independent of the motive and suction enthalpy. The remaining outputs (ER, efficiency, MFRs) are dependent on all variables and characteristic length scales, except on suction enthalpy. The independence of mass flow rates on suction enthalpy is believed to be due to the small differences in gas density as a function of enthalpy. This suggests that suction enthalpy can be neglected as a feature for future models as long as the ejector entrains primarily vapor.

5.1.4. Optimization of performance zones

The gradient descent optimization algorithm, see Section 3.2, was used with the GPR model to identify optimal operating regions for the ejector. As an illustration, the algorithm was tasked to optimize motive pressure and enthalpy with other conditions kept constant. A set of ten initial points were randomly sampled from the distribution between +1 and −1 standard deviation from the mean. These initial points were used in the gradient descent optimizer for ejector efficiency. By plotting a line from each starting point to its optimal value, the optimization steps can be visualized. This is shown in Fig. 5, where the optimization paths from random points in the motive P-h diagram and constant conditions P_s = 38 [bar], Plift = 7 [bar] are shown.

Fig. 5 shows that, for all initial positions, the algorithm is able to improve ejector efficiency and find a close to the optimal operating point. The algorithm converges to solutions in the range of 110–112

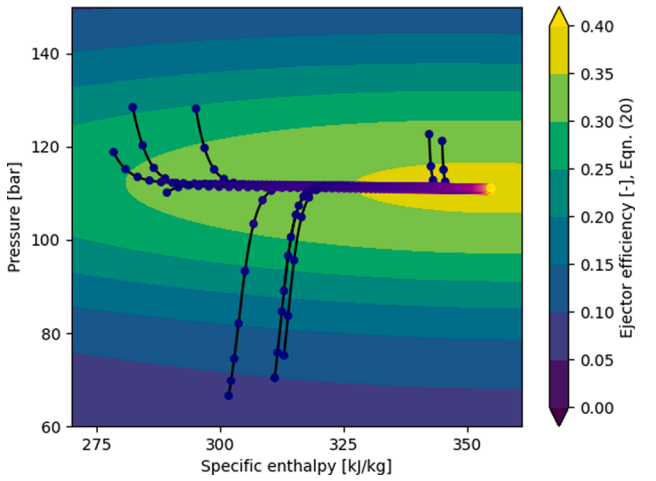

Fig. 5. Optimization paths in a P-h diagram of ejector efficiency from randomized starting positions. Operating conditions: $P_s = 38$ [bar], Plift = 7 [bar] are shown. The optimization path is colored black, and every tenth iteration it plotted with a circle colored according to the iteration number to illustrate convergence.

[bar] for motive pressure P_m and 325–370 [kJ/kg] motive enthalpy h_m with ejector efficiency of 36%. This demonstrates that the algorithm can efficiently find optimal operating conditions using the GPR surrogate model.

5.2. Case 2: Design mapping

Case 2 presents a method of design mapping and optimization of ejector geometry at a given operating condition. In this study, 5 geometric features were included and allowed to vary as presented in Table 2. The choice of geometric dimensions was based on findings from previous studies [7]. This study is limited to 5 geometric features due to the computational costs of sampling additional dimensions. The remaining geometric parameters are set according to the design in Table 3. The operating condition for design optimization is intended for heat pump use cases. With a gas-cooler temperature of 30 °C, the optimal motive pressure is calculated to approximately 85 [bar] using the correlation by Kauf [40]. Suction pressure is set according to the conditions typically found in such applications. The design point is therefore set to: $P_m = 85$ [bar], $T_m = 30[^\circ C]$, $Ps = 33$ [bar], $T_s = -2[^\circ C]$, $P_{\text{lift}} = 5$ [bar].

5.2.1. Database sampling

An initial database of 300 points was generated using LHC sampling. The calculation of this database took approximately 10 days of computation time on a 32 core computer. Due to the small range of positively performing ejectors ($D_{\text{throat}} < D_{\text{mix}} < 3D_{\text{throat}}$), a second database was sampled based on the results from this first database. In this work, new limits were found manually by inspecting the dataspace, however, this procedure can in the future be automated and use an iterative approach to find the best efficiency ejector geometries.

A secondary database of 200 data points was generated with new limits chosen based on the first iteration. The limits of the first and second databases are shown in Table 6. The main reason for the resampling was that the mixing chamber diameter, being the primary factor influencing the entrainment ratio, dominated the effects of the other parameters due to its large sampling range. The mixing chamber diameter limits were therefore reduced to a range where less variation and all of the positive ER geometries were located. The calculation of this second database took approximately 5 days of computation time on a 32 core computer. The model was fitted to the data set and the accuracy was evaluated with a test set of 15% of the data points, similarly to Section 5.1.1. Based on the test data the average absolute error for entrainment ratio value was 0.07 [–]. The following results are discussed with the second iteration database.

Table 6
First and second iteration sampling range.

Parameter	a_{min}	a_{max}
First sampling		
$D_{\text{m-o}}$, [mm]	D_{throat}	1.5 D_{throat}
L_{mix}, [mm]	0	50 D_{mix}
D_{mix}, [mm]	D_{throat}	10 D_{throat}
D_{diff}, [mm]	D_{mix}	10 D_{mix}
α_{d}, [°]	1	90
Second sampling		
$D_{\text{m-out}}$, [mm]	D_{throat}	2 D_{throat}
L_{mix}, [mm]	0	10 D_{mix}
D_{mix}, [mm]	D_{throat}	4 D_{throat}
D_{diff}, [mm]	D_{mix}	10 D_{mix}
α_{d}, [°]	1	90

5.2.2. Model prediction

First, each feature size is varied with the remaining features set constant according to their baseline values (Table 3). The GPR model predicted efficiency is then plotted as a function of each feature size, non dimensionalized by its maximum value, shown in Fig. 6a and b. Both figures show the ejector efficiency under single variable variations using different samples from the GPR function space. This is to illustrate that different realizations of the GPR will converge to different solutions. These results show that optimizing each of these dimensions in isolation can yield significant efficiency improvements. The mixing chamber diameter is very sensitive to optimization and shows a narrow zone of high efficiency. This trend is found in both samples of the GPR model. Similarly, the same functional relationship for mixing chamber length is found in both samples. The diffuser angle relationship is similar for both function samples, however, the optimum value is slightly different. This indicates that more data should be collected in the range of small diffuser angles. The relationship for the motive outlet diameter suggests that only this diameter has only a minor influence on performance. However, as the motive outlet diameter is increased, the ejector performance is reduced, likely due to shock-losses caused by motive flow over-expansion. The predicted performance curve with varied diffuser outlet diameter is different between the two samples, which indicates that the database contains too little information on the relationship to separate from the dominant features; D_{mix}, L_{mix}, and α_d.

Using the combined information from these two samples, the optimal motive outlet diameter from sample B and the optimal outlet diameter from sample A, the individually optimized size of each design parameter was found to be; $D^o_{\text{m-out}}$ =1.78 [mm], $D^O_{\text{mix}} = 3.98$ [mm], $L^O_{\text{mix}} = 23.0$ [mm], $\alpha^O_d = 11.6°$, $D^O_{\text{diff}} = 28.1$ [mm] with a predicted efficiency of 0.42–44 (–). In comparison, the baseline design has a predicted efficiency of 0.40 [–]. The superscript *o* indicates optimum values by isolated optimization. Such a design lies remarkably close to the initially designed ejector (Table 3) in terms of mixing chamber length and diameter.

The motive outlet diameter of an ejector is designed such that the motive nozzle expansion matches the ejector mixing chamber pressure. This achieves the best efficiency as there are lower losses associated with the under- and over-expansion of the motive flow. The individually optimized motive outlet diameter is therefore expected to lie close to this point. As each data point corresponds to a CFD simulation, it is possible to inspect individual ejector data points in detail to investigate this hypothesis. A data point with a motive outlet diameter of 1.77 [mm], close to $D^o_{\text{m-out}}$, is chosen from the database and the pressure

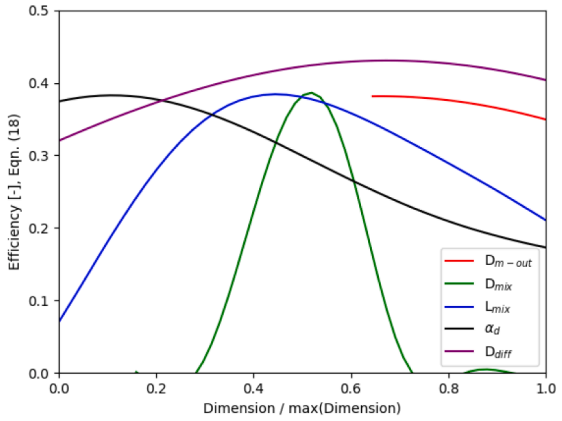

(a) Sample A. Solid line shows predicted efficiency with each dimension varied in isolation. X-axis is non-dimensionalized with the maximum value in the range. Seed 40.

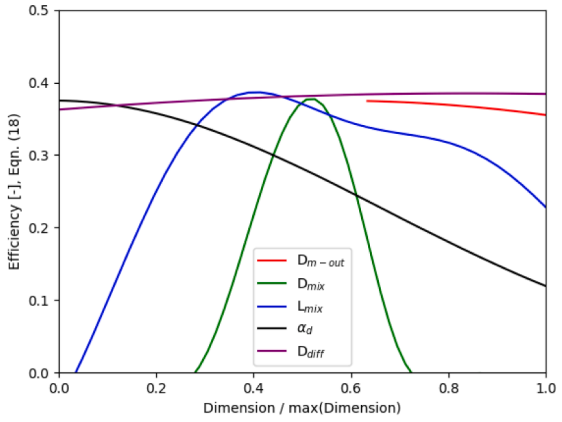

(b) Sample B. Solid line shows predicted efficiency with each dimension varied in isolation. X-axis is non-dimensionalized with the maximum value in the range. Seed 33.

Fig. 6. Plot of ejector efficiency with each dimension varied in isolation with the remaining dimensions left constant as the individual optimum values. Two different randomization seed samples for the training data sets.

profile is shown in Fig. 7. The motive expansion pressure matches the ejector mixing chamber pressure within 1 [bar], illustrating that the algorithm is able to find reasonable design parameters and demonstrating how the database of CFD results can be used to investigate design improvements.

5.2.3. Optimization of design

From previous studies [15,14], it is generally agreed that optimal ejector geometry must be found by optimizing the different parameters of the ejector geometry simultaneously. To better understand the relationships between each design parameter, a performance heat map was generated based on two geometry parameters at a time. As an example, the ejector efficiency for varying mixing diameter and lengths is shown in Fig. 8a with the remaining parameters left constant at the values obtained by single variable optimization. A high efficiency zones is identified near the previous optimal values at $D_{\text{mix}} \approx 4$ [mm] and

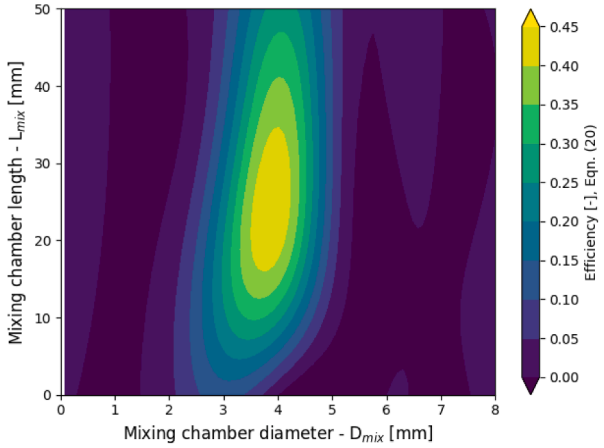

(a) Efficiency contour plot in a D_{mix}-L_{mix} design space. Other parameters kept constant at the individually optimized geometry parameters.

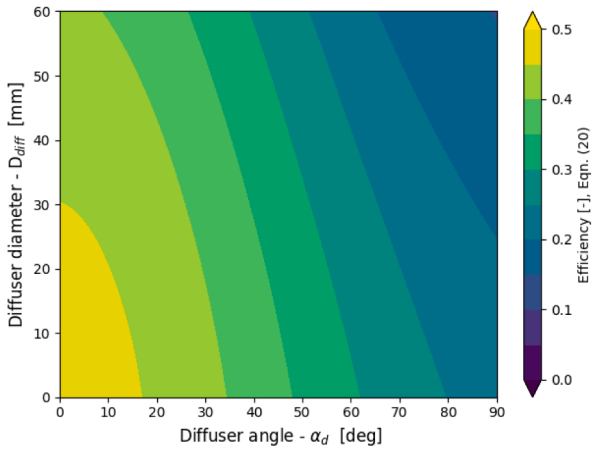

(b) Efficiency contour plot in a α_d-D_{diff} design space. Other parameters kept constant at the individually optimized geometry parameters.

Fig. 8. Efficiency plot of GPR design space prediction.

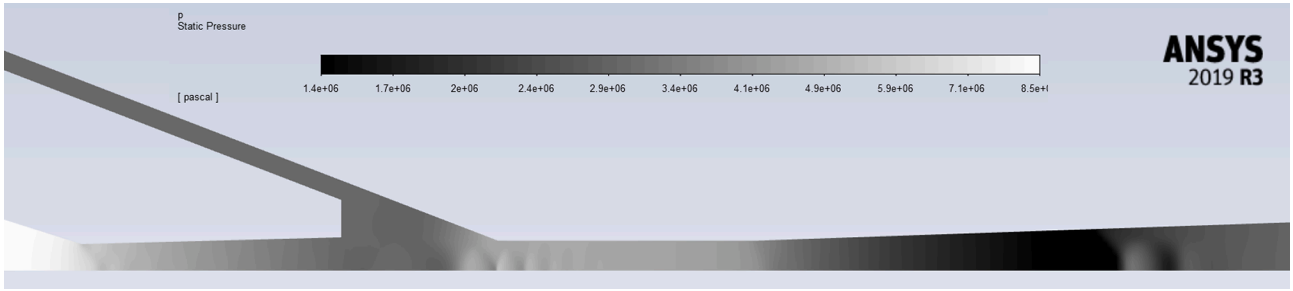

Fig. 7. Pressure distribution for datapoint #46 with dimensions: D_{m-out} =1.77 [mm], D_{mix} = 1.59 [mm], L_{mix} = 6.9 [mm], $\alpha_d = 3.9°$, D_{diff} = 11.9 [mm]. The gray-color scale is log-scaled.

$L_{mix} \approx 25$ [mm]. The predicted ejector efficiency at varied diffuser geometry parameters (α_d, D_{diff}) with remaining parameters as the individual optimum values is shown in Fig. 8b. These results indicate that outlet diameters in the range of 0–20 [mm] and small diffuser diverging angles yield the highest efficiency. Further investigation with a refined database for this region of diffuser geometries is left for future work.

The designs suggested by inspection using the GPR methodology suggests designs with similar dimensions to the initial baseline design. This gives a good indication that the algorithm suggests designs that comparable to designs produced by 1D approaches [41] within a few iterations of database generation. With additional iterations of database refinement, the algorithm is believed to converge to a better, more accurate representation and a better design. A validation of the surrogate model optimized design is conducted in Section 5.2.5.

A more general approach to design optimization is to use an optimizer function on the GPR model. The gradient descent method, as described in previous sections, was used on the GPR model for design parameters. 10 initial points were sampled and optimized for maximizing ejector efficiency. The gradient descent path was constrained such that the ejector optimization algorithm would not suggest negative lengths or angles. The results are presented in Table 7. Of the 10 initial conditions, 8 ended up at the same solution with an efficiency of 43%. The remaining 2 simulations found local optimums with very poor efficiency. The optimized solution converges to a solution close to the previously mentioned individually optimal solution. To improve the design further additional sampling of the database is necessary, which is left to further work.

5.2.4. Design mapping - characteristic length scales

Similarly to Section 5.1.3, the optimized characteristic length scales associated with each geometric design parameter for the prediction of the different KPIs are investigated, shown in Table 8. Some self-evident relationships are apparent from the data. Firstly, the motive mass flow rate is not dependent on the geometry features downstream of the nozzle due to supersonic choking, and the dependency on motive outlet diameter is negligible for this range of motive outlet diameters. As the motive mass flow rate is approximately independent of the model features, the suction mass flow rate, entrainment ratio, and efficiency are closely connected. These features are primarily dependent on the mixing chamber geometry (D_{mix},L_{mix}) and the diffuser angle, which agrees with the previous experimental findings [6,7]. The outlet flow uniformity for velocity and void-fraction is, as expected, dependent only on the diffuser geometry. Lastly, the entropy production in the mixing chamber is primarily governed by the mixing chamber geometry. Further study into these parameters should be conducted in the future to better understand these relationships.

5.2.5. CFD simulation of the optimized ejector design

The CFD predictions with the optimal ejector design may not necessarily agree with the GPR performance predictions. To verify the performance of the GPR optimization, three designs with high predicted ejector efficiency were evaluated with new CFD simulations. The tested designs and the resulting predictions are shown in Table 9 and Fig. 9. The model predictions were very close to the CFD results for all three points, with less than 6% maximum deviation. Additionally, the correct trend is predicted and the best entrainment ratio is found for the optimized design. This very good agreement confirms that our novel approach is a highly useful tool for optimization studies.

Table 7
Optimized designs based on gradient descent

#	D_{m-out} [m]	D_{mix} [m]	L_{mix} [m]	α_D [°]	D_{diff} [m]	Efficiency [–]
1	0.0016	0.0039	0.024	2.4	0.028	0.43
2	0.0016	0.0039	0.024	2.4	0.028	0.43
3	0.0022	0.0059	0.038	78.2	0.004	0.01
4	0.0016	0.0039	0.024	2.4	0.028	0.43
5	0.0016	0.0039	0.024	2.4	0.028	0.43
6	0.0016	0.0039	0.024	2.4	0.028	0.43
7	0.0016	0.0039	0.024	2.4	0.028	0.43
8	0.0022	0.0058	0.000	15.4	0.037	0.02
9	0.0016	0.0039	0.024	2.4	0.028	0.43
10	0.0016	0.0039	0.024	2.4	0.028	0.43

Table 8
Optimized characteristic length scales for different outputs. Kernel seed = 8

Output parameter	Optimized characteristic length scale for feature				
	D_{m-out}	D_{mix}	L_{mix}	α_D	D_{diff}
ER [–]	9.22	1.68	1.18	5.48	30
Efficiency [–]	7.09	0.48	1.36	1.95	27.8
MFR_m [kg/s]	30	30	30	30	30
MFR_s [kg/s]	9.31	1.65	1.18	5.45	30
γ_u [–]	30	30	18.4	15.9	0.585
γ_ϕ [–]	30	30	18.4	15.9	0.585
ds_m-d [–]	30	0.13	7.03	30	30

5.3. Case 3 - Flow structures

The large databases of CFD contains additional information on the 2D flow structures that occur in the ejector. Analysis of the flow structure is in general a challenging problem due to the lack of clear distinctions of flow regimes and regions. As an example, the assumption of two distinctive motive and suction flows that exchange momentum is common in 1D models, however with detailed multidimensional CFD data such a distinction may not exist. Still, detailed knowledge of flow structures and how these vary with changing operating conditions and ejector design is highly valuable for the design process.

Case 3 presents a novel application of the GPR model, namely, to predict the internal flow structures of the ejector using the detailed CFD data. Here, the study is limited to investigating the pressure and velocity along pathlines of the motive and suction flow.

The flow structure inside the ejector is analyzed and mapped along particle pathlines inside the ejector where the curve length parameter, c, is used as a parameter for the GPR model. The velocity and pressure data along these pathlines from the CFD simulations are then used to train the GPR model. By training the GPR model with different ejector design parameters the flow structures can be analyzed as a function of the ejector design. In comparison to predicting the performance KPIs, this is a much harder problem due to the GPR model not having any knowledge of the flow physics. This tool will therefore primarily be used to gain insight into the trends of the ejector flow structures.

The pathlines of the suction and motive flow are illustrated in Fig. 10. Due to the large amount of data available in each CFD simulation, a small database with 25 CFD data points was generated. This database was uniformly sampled over the mixing chamber diameter and mixing chamber length design space in the ranges $10 < L_{mix} < 50$ [mm] and $3 < D_{mix} < 5$ [mm], respectively. The pathlines are defined from the suction and motive inlets to the ejector outlet. Along these pathlines, the different flow variables are reported and post-processed by the algorithm. As the number of data points along each pathline is in most cases several thousand, the data was reduced by averaging over increments of

Table 9
Comparison of entrainment ratio between GPR prediction and CFD model for optimized designs. $D_{m-out} = 1.77$ [mm], $D_{mix} = 3.82$ [mm], $D_{diff} = 65.1$ [mm].

Geometry	#1	#2	#3
L_{mix} [mm]	13.47	27	27
α_D [°]	15.8	15.8	5.0
ER GPR	0.601	0.714	0.742
ER CFD	0.598	0.753	0.793

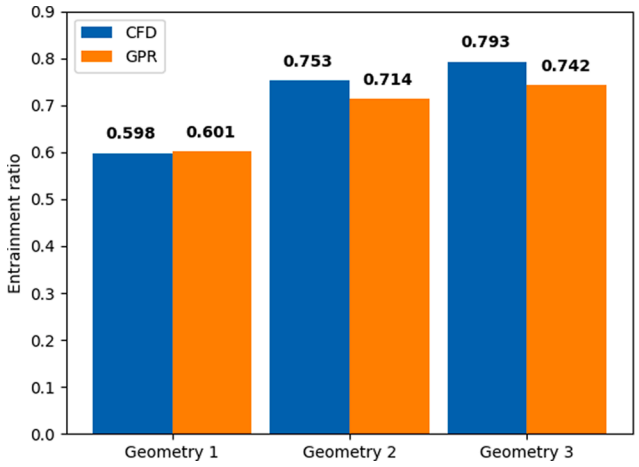

Fig. 9. Comparison of entrainment ratio predicted by the GPR model and new CFD validation points with geometries given according to Table 9.

30 steps along the pathline.

The GPR model is trained to predict the flow variable distributions along the different pathlines. The mixing chamber geometry parameters and the pathline length parameter are chosen as the model features. Fig. 11a–b shows a scatter plot of the CFD data and the predicted pressure along the central suction flow pathline. The CFD data for that geometry was hidden for the GPR predictor to verify the model accuracy when interpolating between ejector geometries. Even with the specific predicted geometry data hidden, a decent match between the CFD data and the predicted velocity and pressure distribution with a mean velocity error of 2.2 [m/s] and 0.13 [bar]. In Fig. 11a, the general pressure structures are reproduced with high accuracy. The method captures the pressure drop occurring in the mixing chamber due to a motive shock train. Still, the predicted shock strength for the smallest mixing chamber length, Fig. 11b, is not well resolved and the shock strength is overpredicted by approximately 2 [bar]. This is likely due to the short length scales and discontinuities along the path line.

A detailed insight into the effects of different design choices on the flow structure is useful for ejector design. This model can give a prediction of the changes to the local flow variables, such as velocity and pressure distributions, as a function of different design variables. An example of such an application is shown in Fig. 12a and b. Fig. 12a shows the predicted velocity along the central suction flow pathline as a function of the mixing chamber diameter for a constant mixing chamber length of 30 [mm]. The figure shows that the highest velocities are achieved with the smallest diameters due to the constricted size of the mixing chamber. For the smallest ejector diameters ($D_{mix} = 3-3.5$ [mm]), the suction MFR (ejector efficiency) is limited by the suction flow area. As the mixing chamber diameter is increased, the suction flow velocity in the ejector is reduced due to the larger flow area and the lowered mixing efficiency. At a mixing diameter of 4 [mm], the maximum ejector efficiency is reached, where the optimal compromise between mixing efficiency and flow area is found. Fig. 12b shows the predicted velocity as a function of the mixing chamber length for a mixing chamber diameter of 4 [mm]. In this data set, the shortest mixing sections were associated with the highest ejector efficiency. As the mixing chamber length is increased, the velocity of the suction flow is reduced and the high-velocity region is extended. For mixing chambers longer than 30 [mm], the predicted velocity distribution in the mixing section is flattened out. This implies that less momentum is transferred from the motive to the suction flow and that the only effect of extending the mixing section beyond 30 [mm] is increasing wall friction.

The presented methodology allows insight into design decisions on a flow structure level. The method can be used as a tool to better predict different flow structures and losses in the ejector. Still, accurately predicting sharp gradients such as shocks is a major challenge for the methodology. Therefore, to produce accurate predictions of flow structures large data sets are needed due to the larger variation of flow structures between ejector geometries and operating conditions.

5.4. Discussion

This approach to ejector mapping and optimization shows great promise both for off-design performance mapping, design mapping, and shape optimization. The algorithm is able to identify high-efficiency regions in design and operating conditions. The algorithm can identify optimized designs, and can by iteration be improved to sample appropriate ranges of data. In addition, the benefits of using CFD data for data points are used to verify ejector designs and investigate flow structures in ejectors. However, some limitations of this modeling approach should be addressed in further work, discussed below.

5.4.1. CFD model accuracy

The GPR machine learning model can only be as good as the data collected. In this study, we have assumed that the CFD results are deterministic, i.e. that the same calculation will always yield the same result. However, due to numerical errors, this cannot be guaranteed. Numerical errors due to poor convergence, poor mesh, or numerical solution errors can affect the CFD model results. This is even more significant if a larger database using data from various sources, such as numerical and experimental data collected from the literature. Ejector meshing is a significant source of numerical errors. Consistent meshing between different ejector designs is challenging due to the large variation in shape and proportions occurring within possible ejector configurations.

Furthermore, the accuracy of the underlying CFD models must be taken into account. As found in previous works [5], the motive nozzle MFR can be quite accurately predicted in the supercritical region, where

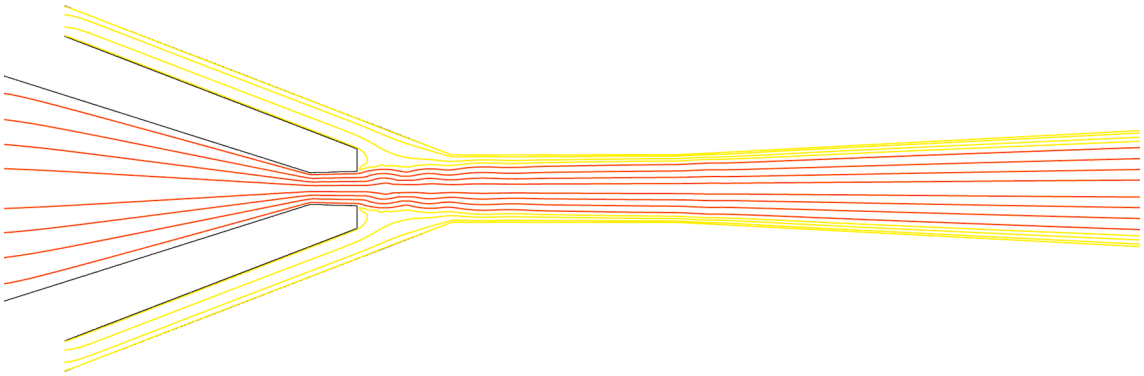

Fig. 10. Illustration of the pathlines of the suction (colored yellow) and the motive (colored red) flows.

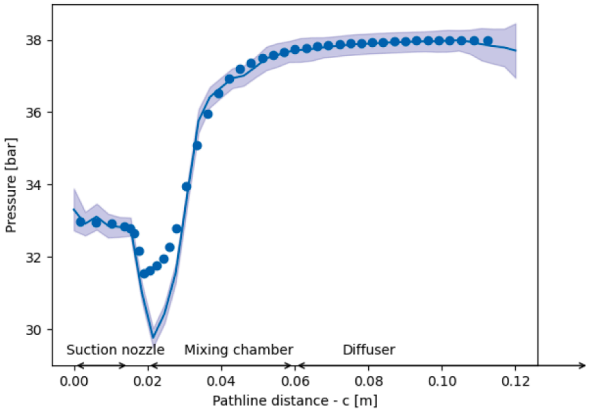

(a) Predicted pressure distribution (line plot) for mixing chamber length $L_{\text{mix}} = 0.01$ [m] along the central suction pathline with the data for the specified geometry hidden to the model.

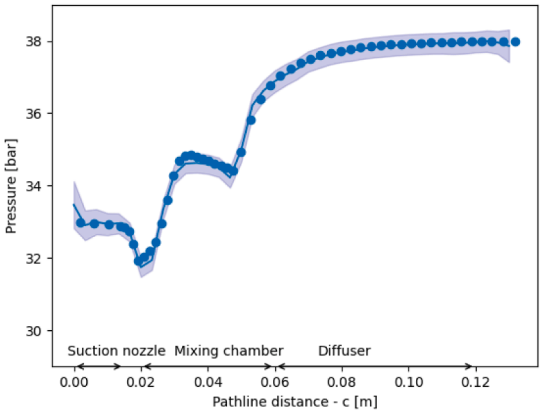

(b) Predicted pressure distribution (line plot) for mixing chamber length $L_{\text{mix}} = 0.03$ [m] along the central suction pathline with the data for the specified geometry hidden to the model.

Fig. 11. Predicted velocity distribution (line plot) along the central suction pathline for two geometries with a mixing chamber diameter of $D_{\text{mix}} = 0.004$ [m]. Verification CFD data marked with circles. The colored area correspond to the predicted velocity +− 1 standard deviation.

this study has been primarily focused. However, the suction flow is often less accurately predicted. Up to 20% error between experimental and numerical results can be observed. This will have a significant impact on the accuracy and validity of the optimized design. Further research into suction flow prediction is necessary to fully leverage the potential of these optimization models. In this work, the motive pressure has been kept above critical to ensure that the HEM accurately represents the flow physics. However, as the motive pressure is reduced, non-equilibrium effects become dominant and must be taken into account. As there is a strong ongoing research effort on this topic, the authors fully expect that numerical methods will soon handle non-equilibrium effects with similar performance as the HEM in the supercritical region. The method developed here will be immediately able to profit from these developments. Accurate prediction of flow separation in the ejector is highly dependent on the CFD model accuracy. Wall shear stress in a turbulent multiphase flow is very complex and is highly dependent on specific CFD model choices, such as wall-mesh resolution and turbulence wall models. This makes the prediction of flow separation highly challenging and should be further investigated in future works.

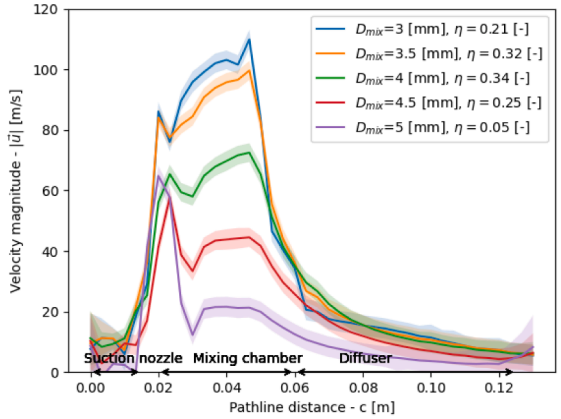

(a) Predicted velocity distribution (line plot) along the central suction pathline as a function of mixing chamber diameter. Mixing chamber length set to $L_{\text{mix}} = 30$ [mm].

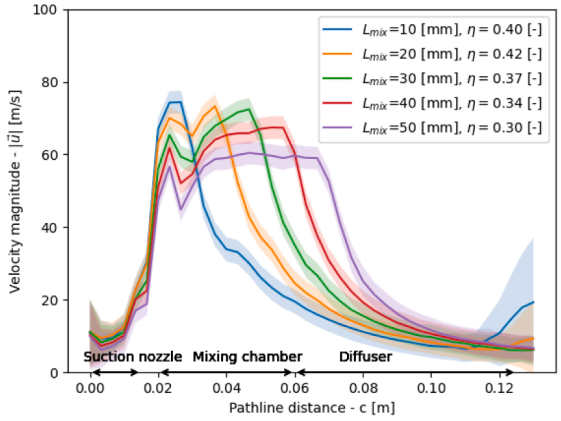

(b) Predicted velocity distribution (line plot) along the central suction pathline as a function of mixing chamber length. Mixing chamber diameter set to $D_{\text{mix}} = 4$ [mm].

Fig. 12. Predicted pressure distribution (line plot) along the central suction pathline for two geometries. Verification CFD data marked with circles. The colored area correspond to the predicted pressure +- 1 standard deviation. Approximate locations of the different ejector sections is shown on the x-axis. Ejector efficiency for each design shown in the figure legend.

5.4.2. GPR modelling

The GPR modeling approach has proven to be able to accurately reproduce CFD-generated ejector performance maps in various configurations. However, the GPR modeling method is sensitive to user errors, poor data, and outliers. It is important to be critical to the model prediction as this is a meta-model, meaning that it makes predictions based on previous model results, which can amplify errors. This work has shown that an appropriate choice of data sampling range is important for optimization, and previous knowledge should be implemented in the model at an early stage. Additionally, that the sampling range and number of data points should be chosen with care. Model accuracy is highly dependent on the number of data points. It is also key to sample such that the mean lies close to the optimal design. In this work, all features were sampled with equal density by the LHC method. This is not optimal as the different features contain different amounts of information about the different KPIs. In further work, alternative data-efficient and adaptive sampling strategies should be explored. The number of required data points scales with the number of features sampled. This study has used 5 features for each use case due to the exponentially

increasing computational costs per additional feature. The number of features and the number of data points should be chosen on a case-by-case basis. Future studies are suggested to explore feature space optimization by use of, for example, Principal Component Analysis (PCA). This could reduce the number of dimensions and the number of data points.

In this work, an iterative approach to data sampling was used based on manual inspection of the data. Further work should investigate the effect of automatically identifying high-performance regions and adaptively sample those regions. This approach can, using the GPR model, be combined with estimated uncertainty to ensure that the optimal data-point distribution is obtained. While the generation of the 200 point database took 5 days of computation time, the method is trivially extendable to large computing clusters as the simulations of different data points are independent.

5.4.3. Flow structure analysis

A challenge that has been highlighted in the literature on response surface modeling for ejectors is the sharp gradients that occur in the design space [42]. The nonlinearities and discontinuities that occur in super-sonic ejectors are challenging to capture with simple regression methods. The GPR methodology can account for several of these structures and non-linearities, however still needs high data density in regions with large gradients for accurate predictions. The use of GPR for these predictions can be further applied to predict the 2D or 3D flow structures as well. However, as the amount of data scales rapidly with additional dimensionality, it is expected to be computationally inefficient. One of the main challenges with such an approach is the large variation in flow structures that occur inside ejectors. These structures may furthermore change abruptly with ejector design or operating conditions. Examples of such conditions are the large gradients associated with the thermodynamics near the critical point of the working fluid or the on-set of supersonic flow.

5.5. Open access tool - GPR model and data

The resulting dataset and GPR model are openly available online. The GPR prediction tool is available as Python 3.9 code based on the Scikit package [29]. The data is openly available for other researchers, and further analysis of and extensions to the databases of ejector data is encouraged. The data is organized as Comma Separated Value - files with all available geometry parameters, operating conditions, flow variables along pathlines, and KPIs. For more details regarding the use of the GPR model in Scikit, see Pedregosa et al. [29]. https://github.com/knutringstad/Ejector_GPR

6. Challenges and further work

This work has demonstrated the possibility to use machine learning on large CFD model databases for component optimization. The primary application for this algorithm is for CO_2 (R744) two-phase ejector design, but may easily be adapted for other working fluids or single-phase ejectors. In future work, the algorithm should be optimized to minimize user input and be close to fully automated. One such method would involve determining several ejector geometry parameters based on predetermined requirements. For example, the motive throat diameter can be determined to produce a given mass flow rate at a certain pressure. The motive outlet diameter can be chosen such that the motive nozzle expansion perfectly matches the mixing chamber pressure, and the outlet diameter such that the outlet velocity is below a certain value. An optimized set of ejector dimensions or a combination of dimensions, could be chosen as features and iteratively and adaptively sampled to optimize ejector operation. The current model optimizes for a single operating point, however, it is possible to optimize performance at a range of operating conditions simultaneously.

Looking forward, it is possible to consider using this approach to cover a combination of operating conditions and ejector geometry. This has the potential to optimize ejector performance and design in all possible combinations. However, this will require a large dataset. Such a dataset could be generated by combining available ejector data from experimental and numerical investigations found in the literature.

The performance maps generated in this work can be implemented into system scale dynamic simulations, similarly to the work by Haida et al. [11] for a multi-ejector module. The presented methodology can for such applications be adapted to the specific ejector geometry and operating conditions of the system, which may increase model accuracy.

Another potential application of the GPR model is to investigate CFD model error prediction, both in comparison to experimental data and in terms of mass conservation. Lastly, it is noted that this approach is generic and can be used for many other applications and components, both for optimization and performance mapping.

The use of GPR analysis in combination with CFD data shows promise as a methodology for predicting flow structures in the ejector. Future work should further explore alternative methods for analyzing the flow data. The prediction of flow separation in the ejector suction chamber and diffuser could be an important tool to avoid losses in the ejector. This could be predicted by analyzing the flow vorticity inside the different ejector sections, or by analyzing the wall shear stress. Additional analysis of mixing efficiency and momentum transfer is of interest and could be analyzed by looking into the jet boundary layer inside the ejector [43]. Another application for the GPR methodology is for the prediction of the different sources of entropy production. By analyzing the local sources of entropy production, such as viscous dissipation and heat transfer, additional insights into the relationships between entropy production and ejector design could be gained [39,44] and further analyzed using GPR. Though the GPR model struggles with capturing the strength and location of super-sonic shock distributions in the ejector, further work should be dedicated toward alternative methods for predicting shock and their related losses in the ejector. As presented in this paper, these flow structure analyses can be introduced into the GPR model either as a KPI or as a local flow variable predicted along the ejector dimensions.

A further application of the flow structure prediction tool is for CFD computation speed-up. As the general structure of several main flow variables can be predicted, the data may be used as initial conditions. This may allow CFD calculations to converge faster as the initial state is closer to the converged solution. Further work should investigate the possibility of including such a method for computational speed up.

7. Conclusions

In this work, the GPR machine learning tool for R744 two-phase ejector design has been trained using large databases of CFD data. An automated algorithm for the generation of CFD databases is presented and used to produce databases of high-quality CFD data for ejectors at various ejector operating conditions and geometries. The data is used to train a GPR model for three cases. First, a performance map of an ejector at various pressure and temperature operating conditions is presented. The model is able to reproduce CFD data for entrainment ratio with $+-0.1$ [–]. Secondly, a mapping of ejector performance factors with various ejector geometries was generated using the surrogate model with similar accuracy within an entrainment ratio of $+-0.07$ [–]. A gradient descent optimization algorithm was implemented and used to optimize ejector operation and ejector design. The final ejector design was found to have an ejector efficiency of 43%. Further improvements could be gained by increasing the number of data points in regions of high efficiency. Last, the GPR model was applied for flow structure prediction from the local CFD data using a database with varied mixing chamber geometries. The method was able to predict different pressure- and velocity structures along the suction flow pathlines within 0.13 [bar] and 2.2 [m/s]. Based on this prediction tool, the optimal combination of mixing chamber length and diameter was analyzed.

To facilitate and encourage further developments with this design method, the data and trained GPR model are made available open-access. Several suggestions for further work have been discussed, where the emphasis is put on the further development of models and methodologies to improve the ejector design process. Improvements to flow structure analysis tools, further study into the details of the machine learning models, and higher accuracy of the underlying CFD models are highlighted topics for future development. By integrating a complete methodology to encompass prediction of ejector performance and flow structures under varied operating conditions and ejector designs, the design of ejectors may in the future be designed quicker, with higher accuracy and a better understanding of design trade-offs.

Declaration of Competing Interest

The authors declare that they have no known competing financial interests or personal relationships that could have appeared to influence the work reported in this paper.

Acknowledgement

The work is part of HighEFF - Centre for an Energy Efficient and Competitive Industry for the Future, an 8-year Research Centre under the FME-scheme (Centre for Environment-friendly Energy Research, 257632). The authors gratefully acknowledge the financial support from the Research Council of Norway and user partners of HighEFF.

References

[1] (RIVM) National Institute for Public Health and the Environment, Contribution of HFCs to the greenhouse effect, 2018. https://www.rivm.nl/en/hydrofluorocarbons/contribution-of-hfcs-to-greenhouse-effect.
[2] European Commision, Regulation (EU) No 517/2014 of the European Parliament and of the Council of 16th April 2014 on fluorinated greenhouse gases and repealing Regulation (EC) No 842/2006, 2014.
[3] S. Girotto, S. Minetto, P. Neksa, Commercial refrigeration system using CO2 as the refrigerant, Int. J. Refrig. 27 (2004) 717–723, https://doi.org/10.1016/j.ijrefrig.2004.07.004.
[4] S. Elbel, N. Lawrence, Review of recent developments in advanced ejector technology, Int. J. Refrig. 62 (2016) 1–18, https://doi.org/10.1016/J.IJREFRIG.2015.10.031, https://www.sciencedirect.com/science/article/pii/S0140700715003266.
[5] K.E. Ringstad, Y. Allouche, P. Gullo, Å. Ervik, K. Banasiak, A. Hafner, A detailed review on CO2 two-phase ejector flow modeling, Therm. Sci. Eng. Prog. 20 (2020) 100647, https://doi.org/10.1016/j.tsep.2020.100647.
[6] M. Nakagawa, A. Marasigan, T. Matsukawa, A. Kurashina, Experimental investigation on the effect of mixing length on the performance of two-phase ejector for CO2 refrigeration cycle with and without heat exchanger, Int. J. Refrig. 34 (2011) 1604–1613, https://doi.org/10.1016/J.IJREFRIG.2010.07.021, https://www.sciencedirect.com/science/article/pii/S0140700710001672.
[7] K. Banasiak, A. Hafner, T. Andresen, Experimental and numerical investigation of the influence of the two-phase ejector geometry on the performance of the R744 heat pump, Int. J. Refrig. 35 (2012) 1617–1625, https://doi.org/10.1016/J.IJREFRIG.2012.04.012, https://www.sciencedirect.com/science/article/pii/S014070071200093X.
[8] J. Hu, J. Shi, Y. Liang, Z. Yang, J. Chen, Numerical and experimental investigation on nozzle parameters for R410A ejector air conditioning system, Int. J. Refrig. 40 (2014) 338–346, https://doi.org/10.1016/j.ijrefrig.2013.12.008.
[9] P. Gullo, M.R. Kærn, M. Haida, J. Smolka, S. Elbel, A review on current status of capacity control techniques for two-phase ejectors, 2020. doi:10.1016/j.ijrefrig.2020.07.014.
[10] M. Haida, J. Smolka, A. Hafner, Z. Ostrowski, M. Palacz, A.J. Nowak, K. Banasiak, System model derivation of the CO2 two-phase ejector based on the CFD-based reduced-order model, Energy 144 (2018) 941–956, https://doi.org/10.1016/j.energy.2017.12.055, https://www.sciencedirect.com/science/article/pii/S0360544217320881?via%3Dihub.
[11] M. Haida, R. Fingas, W. Szwajnoch, J. Smolka, M. Palacz, J. Bodys, A. Nowak, M. Haida, R. Fingas, W. Szwajnoch, J. Smolka, M. Palacz, J. Bodys, A.J. Nowak, An Object-Oriented R744 Two-Phase Ejector Reduced-Order Model for Dynamic Simulations, Energies 12 (2019) 1282, https://doi.org/10.3390/en12071282, https://www.mdpi.com/1996-1073/12/7/1282.
[12] M. Palacz, J. Smolka, W. Kus, A. Fic, Z. Bulinski, A.J. Nowak, K. Banasiak, A. Hafner, CFD-based shape optimisation of a CO_2 two-phase ejector mixing section, Appl. Therm. Eng. 95 (2016) 62–69, https://doi.org/10.1016/j.applthermaleng.2015.11.012, https://www.sciencedirect.com/science/article/pii/S1359431115012478.
[13] M. Palacz, J. Smolka, A.J. Nowak, K. Banasiak, A. Hafner, Shape optimisation of a two-phase ejector for CO2 refrigeration systems, Int. J. Refrig. 74 (2017) 210–221, https://doi.org/10.1016/j.ijrefrig.2016.10.013, https://www.sciencedirect.com/science/article/pii/S0140700716303425.
[14] Y. He, J. Deng, Y. Li, X. Zhang, Synergistic effect of geometric parameters on CO2 ejector based on local exergy destruction analysis, Appl. Therm. Eng. 184 (2021) 116256, https://doi.org/10.1016/j.applthermaleng.2020.116256.
[15] K. Banasiak, M. Palacz, A. Hafner, Z. Buliński, J. Smołka, A.J. Nowak, A. Fic, A CFD-based investigation of the energy performance of two-phase R744 ejectors to recover the expansion work in refrigeration systems: An irreversibility analysis, Int. J. Refrig. 40 (2014) 328–337, https://doi.org/10.1016/j.ijrefrig.2013.12.002, https://www.sciencedirect.com/science/article/pii/S0140700713003812.
[16] Y. He, J. Deng, Y. Li, L. Ma, A numerical contrast on the adjustable and fixed transcritical CO2 ejector using exergy flux distribution analysis, Energy Convers. Manage. 196 (2019) 729–738, https://doi.org/10.1016/j.enconman.2019.06.031.
[17] J. Smolka, Z. Bulinski, A. Fic, A.J. Nowak, K. Banasiak, A. Hafner, A computational model of a transcritical R744 ejector based on a homogeneous real fluid approach, Appl. Math. Model. 37 (2013) 1208–1224, https://doi.org/10.1016/j.apm.2012.03.044, https://www.sciencedirect.com/science/article/pii/S0307904X12002077.
[18] C. Lucas, H. Rusche, A. Schroeder, J. Koehler, Numerical investigation of a two-phase CO2 ejector, Int. J. Refrig. 43 (2014) 154–166, https://doi.org/10.1016/j.ijrefrig.2014.03.003, https://www.sciencedirect.com/science/article/pii/S0140700714000504.
[19] Y. Fang, S. Poncet, H. Nesreddine, Y. Bartosiewicz, An open-source density-based solver for two-phase CO2 compressible flows: verification and validation, Int. J. Refrig. (2019), https://doi.org/10.1016/j.ijrefrig.2019.05.016 https://www.sciencedirect.com/science/article/pii/S0140700719302129#bib0034.
[20] M. Haida, J. Smolka, A. Hafner, M. Palacz, K. Banasiak, A.J. Nowak, Modified homogeneous relaxation model for the R744 trans-critical flow in a two-phase ejector, Int. J. Refrig. 85 (2018) 314–333, https://doi.org/10.1016/j.ijrefrig.2017.10.010, https://www.sciencedirect.com/science/article/pii/S0140700717303948.
[21] R.B. Barta, P. Dhillon, J.E. Braun, D. Ziviani, E.A. Groll, Design and optimization strategy for ejectors applied in refrigeration cycles, Appl. Therm. Eng. 189 (2021) 116682, https://doi.org/10.1016/J.APPLTHERMALENG.2021.116682.
[22] R.B. Gramacy, Surrogates: Gaussian Process Modeling, Design and Optimization for the Applied Sciences, Chapman Hall/CRC, Boca Raton, Florida, 2020 http://bobby.gramacy.com/surrogates/.
[23] A. Maghsoodi, E. Afshari, H. Ahmadikia, Optimization of geometric parameters for design a high-performance ejector in the proton exchange membrane fuel cell system using artificial neural network and genetic algorithm, Appl. Therm. Eng. 71 (2014) 410–418, https://doi.org/10.1016/J.APPLTHERMALENG.2014.06.067.
[24] M.M. Rashidi, A. Aghagoli, R. Raoofi, Thermodynamic analysis of the ejector refrigeration cycle using the artificial neural network, Energy 129 (2017) 201–215, https://doi.org/10.1016/J.ENERGY.2017.04.089.
[25] C. Haoran, C. Wenjian, Artificial neural network modeling for variable area ratio ejector, in, in: 9th IEEE Conference on Industrial Electronics and Applications, 2014, pp. 220–225, https://doi.org/10.1109/ICIEA.2014.6931162.
[26] P. Chaurasia, K. Younis, O.S. Qadri, G. Srivastava, K. Osama, Comparison of Gaussian process regression, artificial neural network, and response surface methodology modeling approaches for predicting drying time of mosambi (Citrus limetta) peel, J. Food Process Eng 42 (2019) e12966, https://doi.org/10.1111/JFPE.12966, https://onlinelibrary.wiley.com/doi/full/10.1111/jfpe.12966.
[27] ANSYS, ANSYS fluent theory guide. Release 19.0., Canonsburg, 2018.
[28] I.H. Bell, J. Wronski, S. Quoilin, V. Lemort, Pure and Pseudo-pure Fluid Thermophysical Property Evaluation and the Open-Source Thermophysical Property Library CoolProp, Ind. Eng. Chem. Res. 53 (2014) 2498–2508.
[29] F. Pedregosa, G. Varoquaux, A. Gramfort, V. Michel, B. Thirion, O. Grisel, M. Blondel, P. Prettenhofer, R. Weiss, V. Dubourg, J. Vanderplas, A. Passos, D. Cournapeau, M. Brucher, M. Perrot, E. Duchesnay, Scikit-learn: Machine Learning in Python, J. Mach. Learn. Res. 12 (2011) 2825–2830.
[30] D.C. Liu, J. Nocedal, On the limited memory BFGS method for large scale optimization, Math. Program. 1989 45:1 45 (1989) 503–528. https://link.springer.com/article/10.1007/BF01589116. doi:10.1007/BF01589116.
[31] C.E. Rasmussen, C.K.I. Williams, Gaussian Processes for Machine Learning, Massachusetts Institute of Technology, 2006.
[32] H. Sit, C.J. Earls, Gaussian Process Regression for Estimating EM Ducting Within the Marine Atmospheric Boundary Layer, Radio Sci. 55 (2020), https://doi.org/10.1029/2019RS006890 e2019RS006890. https://agupubs.onlinelibrary.wiley.com/doi/full/10.1029/2019RS006890.
[33] Software Python Foundation, Python 3.9, 2021.
[34] M. Haida, J. Smolka, A. Hafner, M. Mastrowski, M. Palacz, K.B. Madsen, A. J. Nowak, K. Banasiak, Numerical investigation of heat transfer in a CO2 two-phase ejector, Energy 163 (2018) 682–698, https://doi.org/10.1016/j.energy.2018.08.175, https://www.sciencedirect.com/science/article/pii/S0360544218317110?via%3Dihub.
[35] B. Tang, Orthogonal Array-Based Latin Hypercubes, J. Am. Statist. Assoc. 88 (1993) 1392–1397, https://doi.org/10.1080/01621459.1993.10476423, http://www.tandfonline.com/doi/abs/10.1080/01621459.1993.10476423.
[36] S. Elbel, P. Hrnjak, Experimental validation of a prototype ejector designed to reduce throttling losses encountered in transcritical R744 system operation, Int. J. Refrig. 31 (2008) 411–422, https://doi.org/10.1016/J.IJREFRIG.2007.07.013, https://www.sciencedirect.com/science/article/pii/S0140700707001508.
[37] M. Palacz, J. Smolka, A. Fic, Z. Bulinski, A.J. Nowak, K. Banasiak, A. Hafner, Application range of the HEM approach for CO2 expansion inside two-phase

ejectors for supermarket refrigeration systems, Int. J. Refrig. 59 (2015) 251–258, https://doi.org/10.1016/j.ijrefrig.2015.07.006, https://www.sciencedirect.com/science/article/pii/S0140700715002030.

[38] M. Palacz, M. Haida, J. Smolka, A.J. Nowak, K. Banasiak, A. Hafner, HEM and HRM accuracy comparison for the simulation of CO2 expansion in two-phase ejectors for supermarket refrigeration systems, Appl. Therm. Eng. 115 (2017) 160–169, https://doi.org/10.1016/j.applthermaleng.2016.12.122, https://www.sciencedirect.com/science/article/pii/S135943111634399X.

[39] J. Sierra-Pallares, J. García Del Valle, P. García Carrascal, F. Castro Ruiz, A computational study about the types of entropy generation in three different R134a ejector mixing chambers, Int. J. Refrig. 63 (2016) 199–213, https://doi.org/10.1016/J.IJREFRIG.2015.11.007.

[40] F. Kauf, Determination of the optimum high pressure for transcritical CO2-refrigeration cycles, Int. J. Therm. Sci. 38 (1999) 325–330, https://doi.org/10.1016/S1290-0729(99)80098-2.

[41] K. Banasiak, A. Hafner, 1D Computational model of a two-phase R744 ejector for expansion work recovery, Int. J. Therm. Sci. 50 (2011) 2235–2247, https://doi.org/10.1016/j.ijthermalsci.2011.06.007, https://www.sciencedirect.com/science/article/pii/S1290072911001876.

[42] G. Grazzini, A. Milazzo, F. Mazzelli, Ejectors for efficient refrigeration: Design, applications and computational fluid dynamics, Springer International, 2018, https://doi.org/10.1007/978-3-319-75244-0. URL https://books.google.no/books?hl=no&lr=&id=Vq9SDwAAQBAJ&oi=fnd&pg=PR7&ots=Vza5cXBAC3&sig=UllOPQVfZdvUSThJ4Q4NwIvfjw8&redir_esc=y#v=onepage&q&f=false.

[43] Y. Tang, Z. Liu, Y. Li, Z. Huang, K.J. Chua, Study on fundamental link between mixing efficiency and entrainment performance of a steam ejector, Energy 215 (2021) 119128, https://doi.org/10.1016/J.ENERGY.2020.119128.

[44] F. Kock, H. Herwig, Local entropy production in turbulent shear flows: a high-Reynolds number model with wall functions, Int. J. Heat Mass Transf. 47 (2004) 2205–2215, https://doi.org/10.1016/J.IJHEATMASSTRANSFER.2003.11.025.